Chemical Science

ROYAL SOCIETY OF CHEMISTRY

EDGE ARTICLE

View Article Online
View Journal | View Issue

Cite this: *Chem. Sci.*, 2026, **17**, 1137

All publication charges for this article have been paid for by the Royal Society of Chemistry

Broad-spectrum rejection of emerging organic contaminants with different structures and properties from complex water matrices by a chlorine-resistant Janus nanofiltration membrane

Zebin Hu,† Kaiyue Tian,† Longzhe Li, Han Dai, Zhangbo Peng, Zhonglong Yin * and Weiben Yang

Emerging organic contaminants (EOCs) are causing a global water safety crisis and pollution, while conventional nanofiltration membranes with negative charge are inadequate to remove positively charged EOCs, and their poor chlorine resistance strongly hinders their performance. Herein, Janus membranes (JMs) were tailored to reject EOCs with different structures and properties by firmly incorporating two-dimensional metal–organic frameworks (2D-MOFs) with different sizes and charge characteristics into a chlorine-resistant and porous polyvinylidene difluoride matrix. By adjusting the ligand substitution and synthesis temperature, the pore size, charge and hydrophilicity of the 2D-MOFs were controllably modulated to impart the membranes with high permeability and broad-spectrum removal of positively and negatively charged EOCs (antibiotics, endocrine disrupting chemicals, per- and polyfluoroalkyl substances, and organophosphate esters). The JMs presented superior separation performance compared to single-sided and state-of-the-art nanofiltration membranes owing to the electrostatic Janus structure, and porous and hydrophilic nature of the 2D-MOFs. Notably, the JM200 membrane demonstrated exceptional water permeability (55.6 L per m^2 per h per bar) and rejection of tobramycin, 3,3,5,5-tetrabromobisphenol A, heptadecafluorononanoic acid and tris(2-phenylphenyl) phosphate (over 99.9%). Additionally, the JM200 membrane exhibits outstanding antibiotics/salt selectivity (separation factor of tobramycin/NaCl = 152), anti-fouling, chlorine resistance (chlorine exposure of 400 000 ppm min) and stability, delivering superior performance compared to the commercial NF270 membrane during long-term treatment of real surface water and municipal wastewater. This study opens a sustainable avenue for ultrafast and broad-spectrum removal of EOCs from complex water matrices with low energy and chemical consumption.

Received 7th August 2025
Accepted 6th November 2025

DOI: 10.1039/d5sc05978j

rsc.li/chemical-science

Introduction

Recently, emerging organic contaminants (EOCs), such as antibiotics, endocrine disrupting chemicals (EDCs), per- and polyfluoroalkyl substances (PFAS) and organophosphate esters (OPEs), have posed increasing potential threats to aquatic organisms and human health.[1] Benefiting from high efficiency and sustainable separation, nanofiltration (NF) technology has garnered widespread attention for EOC removal.[2]

Polyamide (PA) thin film composite (TFC) NF membranes synthesized by interfacial polymerization have become a golden standard in desalination.[3] For the purpose of desalination and anti-fouling, they were designed to possess a negative charge owing to the presence of carboxylic groups (–COOH) in the PA active layer, but they were not effective in removing positively charged EOCs ($EOCs^+$) according to the Donnan effect.[4] For example, although EOC^+ pindolol (440 Da) had a much higher molecular weight than that of negatively charged EOC (EOC^-) ibuprofen (206 Da), the commercial NF membrane Desal HL presented a lower rejection of ibuprofen (98.4%) than pindolol (74.2%).[5] Moreover, PA membranes suffer from poor chlorine resistance, which limits the membrane biofouling mitigation.[6]

To overcome the above limitations, intensive efforts have been devoted to constructing positively charged membranes for the removal of $EOCs^+$. Zhao *et al.*[7] prepared positively charged PEI-25k NF membranes, which significantly improved the rejection of EOC^+ enrofloxacin (>93%). However, the rejection of $EOCs^-$ is compromised, and they are prone to fouling by organic foulants.[8] Constructing dually-charged membranes may increase the rejection of both $EOCs^-$ and $EOCs^{4+}$, but it is difficult to control the spacing between positively and negatively

Jiangsu Key Laboratory of New Power Batteries, Jiangsu Collaborative Innovation Center of Biomedical Functional Materials, School of Chemistry and Materials Science, Nanjing Normal University, Nanjing 210023, China. E-mail: 07263@njnu.edu.cn

† Both authors contributed equally to this work.

charged groups in a confined channel, causing electroneutralization.[9] Electrostatic Janus membranes (JMs) hold great potential in synchronous separation of $EOCs^-$ and $EOCs^+$ due to their asymmetric properties. However, JMs feature two functional layers, which complicates the preparation process and increases the membrane filtration resistance, thus sacrificing the permeability.[10] More importantly, EOCs are diverse species (*e.g.*, antibiotics, EDCs, and PFAS) with different structures and properties; meanwhile, they usually coexist with conventional pollutants, which further brings greater challenges for broad-spectrum removal of EOCs from complex water matrices (*e.g.*, surface water and municipal wastewater) by the existing NF membranes. Hence, it is quite urgent and challenging to customize more resilient Janus NF membranes for EOC removal.

Benefiting from well-defined pores, a designable structure and short-range transport channels, two-dimensional metal–organic frameworks (2D-MOFs) have attracted intensive attention in membrane fabrication.[11] 2D-MOFs provide additional and short water channels for superior permeability without compromising selectivity, which can break the permeability-selectivity trade-off.[12] Moreover, the pore structure and properties (*e.g.*, charge and hydrophobicity) of 2D-MOFs can be easily modulated by changing the synthesis conditions, and using diverse metal and organic ligands, potentially making membranes to match EOCs with different structures and properties for removal. However, most of the studies only focus on individual EOC rejection, and there is a huge gap for broad-spectrum rejection of EOCs.

Here, we overcome these bottlenecks by confining functionalized 2D-MOFs into a highly porous and chlorine-resistant polyvinylidene difluoride (PVDF) matrix on two sides of an electrostatic Janus NF membrane *via* facile and scalable phase inversion. $2D\text{-}MOFs^+$ and $2D\text{-}MOFs^-$ were derived from non-noble and environmentally friendly MgAl layered double hydroxides (LDH) with organic ligands 2-amino-terephthalic acid (NH_2–BDC) and terephthalic acid (BDC), respectively. Moreover, their controllable pore size and properties imparted the membrane with a porous and defect-free active layer for ultrafast and broad-spectrum removal of EOCs. Correlation analysis and membrane transport models were employed to understand the rejection mechanism. Additionally, membrane anti-fouling and chlorine resistance performance were further explored. The potential application of the membrane was demonstrated by the treatment of three real water matrices. This study may guide the development of next-generation, more resilient NF membranes for remediation or reuse of EOC-contaminated water.

Materials and methods

Membrane performance test

Reagents and chemicals are provided in Text S1. The fabrication and characterization of the 2D-MOF Janus membranes are described in Texts S2 and S3, respectively. By modulating the organic ligand to BDC and NH_2–BDC, negatively and positively charged 2D-MOFs were obtained and denoted as MgAl–BDC-*X* and MgAl–BDC–NH_2-*X*, respectively; moreover, the fabricated Janus membranes were denoted as JMX, where *X* represents the synthesis temperature of the 2D-MOFs. For comparison purposes, single-sided membranes were also constructed by separately incorporating MgAl–BDC-*X* and MgAl–BDC–NH_2-*X* into a PVDF matrix, designated as SMX-N and SMX-P, respectively, where N and P represent negative and positive charge. A PVDF control membrane was fabricated without adding 2D-MOFs.

The separation performance of the membranes was evaluated using cross-flow filtration equipment (SF-SB, Saifei Instrument, China) as described elsewhere.[13] Before measurement, the membrane with an effective surface area of 0.0034 m^2 was pre-pressurized with DI water for 6 h at the transmembrane pressure (TMP) of 0.2 MPa and a flow rate of 0.22 m s^{-1}.

Rejection of EOCs

The fabricated Janus NF membranes were evaluated by filtering target emerging contaminants (antibiotics, EDCs, PFAS, OPEs) with a wide range of concentrations (50–500 μg L^{-1}) and pH values (5–9). Information on the EOCs is provided in Table S1. To exclude the effect of adsorption on rejection, the 2D-MOF membranes were immersed in feed water containing EOCs for 12 h to ensure adsorption saturation.[14]

Contaminant rejection *R* (%) was calculated using eqn (1).[15]

$$R = \frac{C_f - C_p}{C_f} \times 100\% \quad (1)$$

where C_f and C_p are the concentrations of the contaminants in the feed and permeate water, respectively, and their determination methods are described in Text S4.

Water flux (J_0, L per m^2 per h per bar) was determined using eqn (2).[4]

$$J_0 = \frac{\Delta m}{\rho \times A_m \times \Delta t \times \Delta P} \quad (2)$$

where ρ (g L^{-1}) is the density of permeate water, Δm (g) is the mass of permeable water at a time interval Δt (h) under TMP of ΔP (bar), and A_m (m^2) is the effective membrane area.

The correlation between EOC properties and separation performance was analyzed using SPSS Statistics 17.0 software, as described elsewhere.[16] A rigorous analysis based on established membrane transport principles was supplemented using Ferry's model, Donnan model and Donnan-Steric pore model as described in Text S5.

Anti-fouling test

An anti-fouling test was conducted by filtration of bovine serum albumin (BSA, a model foulant), humic acid (HA) and sodium alginate (SA) with a concentration of 100 mg L^{-1}.[13] The permeate flux is denoted as J_1 after fouling for 1.5 h. The fouled membrane was washed with DI water for 10 min at 2 bar, and the DI water flux (J_2) was tested again. Then the flux recovery ratio (FRR), total fouling ratio (R_t), reversible fouling ratio (R_r), and irreversible fouling ratio (R_{ir}) were determined using eqn (3)–(6), respectively.[17] Besides, the influence of the feed

direction on the fouling performance was investigated for both sides of the JM.

$$\mathrm{FRR} = \frac{J_2}{J_0} \times 100\% \quad (3)$$

$$R_t = \left(1 - \frac{J_1}{J_0}\right) \quad (4)$$

$$R_r = \left(\frac{J_2 - J_1}{J_0}\right) \quad (5)$$

$$R_{ir} = \left(1 - \frac{J_2}{J_0}\right) \quad (6)$$

Chlorine resistance tests

Chlorine resistance tests were performed using a static approach.[6] Briefly, the Janus membrane and commercial NF270 membrane were initially immersed in 50 mg L^{-1} of NaOCl solution (with an available chlorine concentration of 4.99%) under continuous stirring when the pH was adjusted to 7. At specified times, the membranes were taken out of the NaOCl solution and thoroughly rinsed with DI water, and then their separation performance was tested to assess the possible membrane degradation. The total free chlorine (FC) exposure of the NF membranes was calculated as CT_{FC} (ppm min) $= \int C_{FC} dt$, where CT refers to the total concentration of free chlorine. Additionally, a dynamic cross-flow chlorine resistance test was conducted by filtering a TC solution containing NaOCl (50 mg L^{-1}) for 6 h at TMP of 0.2 MPa.

Application in wastewater reclamation

The long-term filtration performance of the Janus membranes was tested by continuously filtrating three typical water matrices for 7 d, including Yangtze River water, Caiyue Lake water and municipal wastewater secondary effluent. The municipal wastewater treatment process is illustrated in Fig. S1. The composition and properties of the feed water are illustrated in Tables S2–S4. The feed water information and operating process are described in Text S6.

Results and discussion

Design of the Janus membranes

Janus membranes were designed by separately incorporating negatively and positively charged 2D-MOFs (2D-MOFs$^-$ and 2D-MOFs$^+$) into a PVDF matrix with high chlorine resistance on two sides of a nonwoven fabric substrate through the nanobubble-mediated NIPS method (Fig. 1a). Nanobubbles (pore size was approximately 1.29 nm, Fig. S2) were generated by a facile sonication step, which served as green porogen for the fabrication of a porous matrix. 2D-MOFs$^-$ (MgAl–BDC) and 2D-MOFs$^+$ (MgAl–BDC–NH_2) were derived from MgAl-LDH with the assistance of BDC and NH_2–BDC, respectively, by a hydrothermal method. Their pore size and hydrophilicity can be modulated by changing the conversion temperature and ligand substitution (–H, –NH_2), respectively. Therefore, the precise control of the size and properties of the 2D-MOFs endowed the membranes with a tunable structure to allow the rejection of different EOCs. Moreover, the highly porous membrane matrix and hydrophilic 2D-MOFs are expected to avoid the high membrane resistance caused by two functional layers, which provides a novel design concept of a chlorine-resistant and highly permeable NF membrane for broad-spectrum rejection of EOCs.

The positively and negatively charged sides of the JM exhibited white and brown colors, respectively, and tolerated bending and folding (Fig. 1b and d). SEM (Fig. S3a–g) and TEM (Fig. S3h) images revealed that the smooth and hexagonal layered MgAl-LDH converted to rough and layered stacks of nanoribbons for the MgAl-MOFs, which was facilitated by the synthesis temperature. Such structures favor the compatibility of the 2D-MOFs with the membrane matrix and form a defect-free membrane surface (Fig. 1c and e), which also enhances the mechanical strength (Fig. S4) by restricting chain mobility.[14] In particular, JM200 possessed the highest yield strength (41.9 MPa) and breaking strength (80.8 MPa). Furthermore, the X-ray diffraction (XRD) patterns and Fourier-transform infrared spectra (FTIR) characterizations confirmed the complete conversion of the MgAl-LDH into MgAl-MOFs. Two distinct diffraction peaks of MgAl-LDH at $2\theta = 11.8°$ ((003) plane) and 23.6° ((006) plane) (Fig. S5a) vanished entirely after combination with organic ligands, accompanied by the appearance of peaks corresponding to 2D-MOFs at $2\theta = 9.0°$ ((101) plane), 9.6° ((220) plane) and 14.2° ((420) plane).[18] Similarly, the bending vibration characteristics of the carbonate between the LDH interlayers (1352 cm^{-1}) disappeared after transformation (Fig. S5b), while peaks emerged for the asymmetric and symmetry stretching of –COO^- in the organic ligand.[19] Meanwhile, the above characteristic crystal peaks (Fig. S6) of the 2D-MOFs were observed on the JMs. Moreover, the cross-sectional morphology of the JMs (Fig. S7) revealed that the integrated 2D-MOF nanosheets were embedded within the alveolar PVDF matrix, and the interface of the 2D-MOFs with the polymer matrix was tight. The uniform distribution of Mg and Al on the two sides of the JM from energy dispersive spectrometer (EDS) mapping (Fig. 1f) further indicated the successful and firm incorporation of the 2D-MOFs into the membrane.

Furthermore, N_2 adsorption–desorption isotherms (Fig. S5c) revealed that the MgAl-MOFs had a much higher specific surface area (154–703 m^2 g^{-1}) than the MgAl-LDH (only 21 m^2 g^{-1}) (Table S5). Moreover, the pore size of the 2D-MOFs (Fig. S5d) decreased with increasing synthesis temperature by facilitating the formation of nuclei and higher-order growth,[20] causing the lower molecular weight cut-off (MWCO, 442.7–880.3 Da) (Fig. S8) and smaller average pore size (0.72–0.99 nm) (Fig. 1g) of the JM. Consequently, the pore size of the JM can be precisely controlled to retain EOCs with different sizes. In comparison, the MWCO of the JM with the same total thickness of the active layer is lower than that of the single-sided membrane (SM) (about 100 Da, Fig. S8), suggesting that the

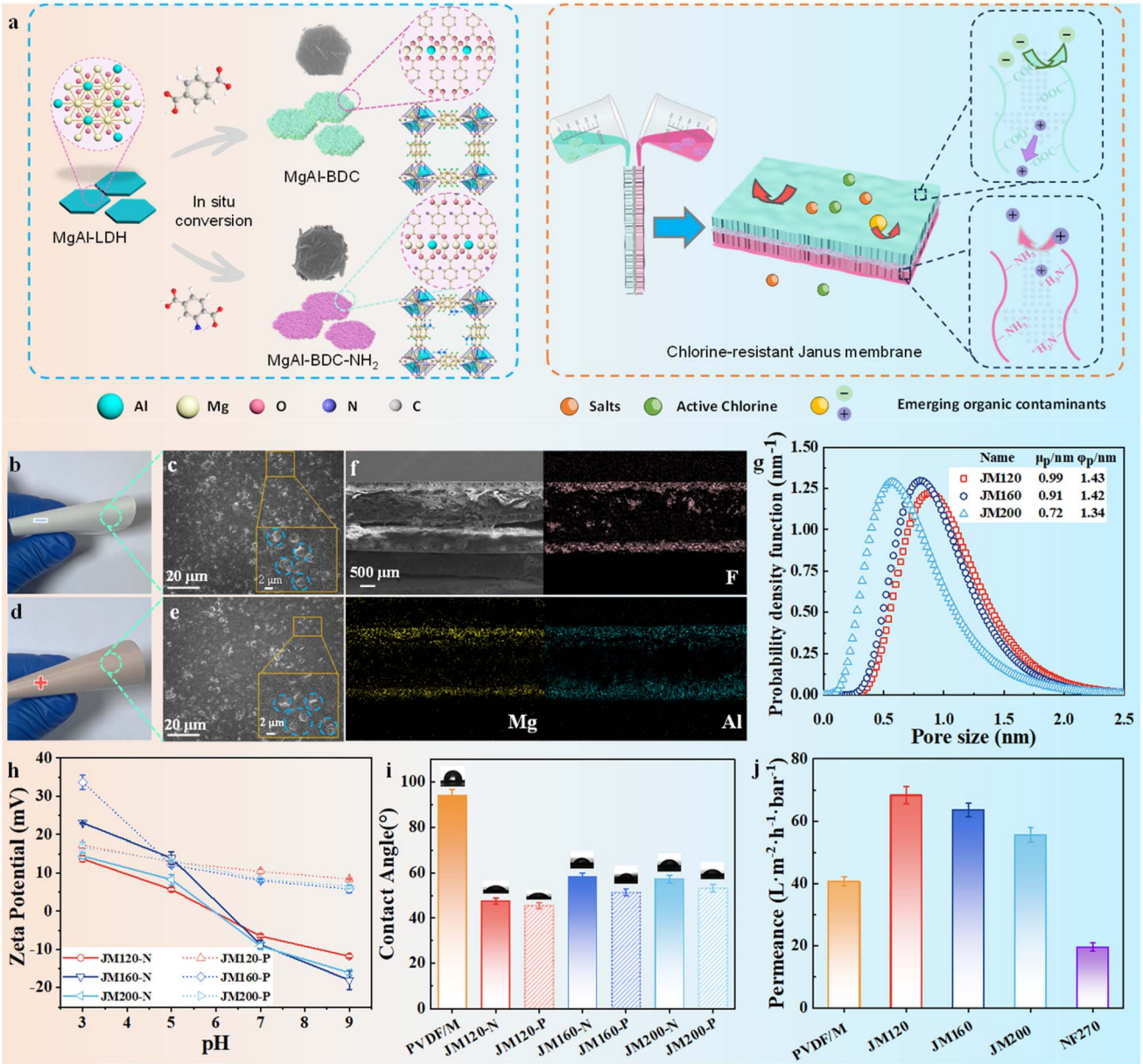

Fig. 1 Design and characterization of the 2D-MOF chlorine-resistant Janus NF membrane. Schematic of membrane fabrication (a), photos and SEM images of the negatively (b and c) and positively (d and e) charged sides in JM200, cross-sectional morphology and corresponding EDS mapping of JM200 (f), pore size distribution (g), zeta potentials (h), water contact angle (i) and pure water permeance of the membranes (j).

two functional layers of the JM healed the defects in the SM and thus favored EOC rejection. In addition, MgAl–BDC and MgAl–BDC–NH_2 imparted the two sides of the JM with negative (zeta potential from −6.52 to −9.13 mV) and positive (zeta potential from 8.03 to 10.4 mV) charges at neutral pH (Fig. 1h), respectively. Consequently, the surface charge of the JM was effectively controlled by adjusting the substitution in the organic ligands. Furthermore, the hydrophilic nature of the MgAl-MOFs imparted the JM with a much lower water contact angle (45.5–58.2°) than the PVDF control membrane (94°) (Fig. 1i). The increased hydrophilicity is conducive to water transport and anti-fouling of the JM.[21] Therefore, the 2D-MOFs imparted the JM with higher pure water permeability as synthesis temperature decreased, owing to the increase in MWCO, ranging from 55.6 to 68.3 L per m^2 per h per bar (Fig. 1j). Notably, the JM presented 2.08–3.25 times higher water permeability than NF270 (a typical commercial NF membrane, active layer thickness = 35 nm (ref. 22)) due to the following reasons: (I) the alveolar membrane matrix presented a highly porous structure; moreover, although the entire functional layer thickness was 600 μm, the true thickness of the thin, dense skin layer at the surface on each side of the JM (actual active layer) was 106–108 nm (Fig. S9), causing low filtration resistance; (II) the 2D-MOFs exhibited a porous and hydrophilic structure, which provided additional channels for water transport after incorporation into the membrane.[23] This allowed for satisfactory flux under low

applied pressure, which significantly reduced energy consumption and favored membrane fouling control since membrane fouling usually becomes more serious at high operating pressures.[24] Besides, Fig. S10 illustrates that the control membrane made without the nanobubble porogen presented a more compact surface of the active layer than the JM, causing much lower permeability (5.4 L per m^2 per h per bar). Overall, by precisely modulating the PVDF matrix and 2D-MOF structure, a Janus membrane was successfully designed with tunable size, charge and hydrophilic properties, and high water permeability. Moreover, the increase in synthesis temperature boosted the nucleation rate, regulated the crystal nucleation and growth,[25] and formed well-developed layered stacks of nanoribbons of the 2D-MOF with a higher specific surface area and lower pore size. Consequently, the facile control of the synthesis temperature of the 2D-MOFs enabled the tunable modulation of the membrane structure. Notably, without the application of the 2D-MOFs, the challenge for traditional positively and negatively charged nanofiltration membranes lies in identifying the optimal ratio of positively and negatively charged monomers and the synthesis conditions. This study will contribute to the development of more durable next-generation NF membranes.

Rejection of EOCs

The rejection of EOCs with different charge properties was determined by the fabricated NF membranes. The 2D-MOFs imparted the JM with superior antibiotic rejection (Fig. 2a and S11) at elevated synthesis temperatures (120–200 °C) owing to the lower MWCO (Fig. S8) and pore size (Fig. 1i) of the membrane. Thus, JM200 (MWCO = 442.7 Da) was favorable to reject antibiotics *via* size exclusion. Notably, the rejection of negatively charged tetracycline (TC, MW = 444 Da), and positively charged erythromycin (ERY, MW = 734 Da) and tobramycin (TOB, MW = 467 Da) reached as high as 99.2%, 100% and 99.9%, respectively, since their molecular weight (MW) was higher than the membrane MWCO. Benefiting from the electrostatic Janus structure, although the MW of negatively charged sulfamethoxazole (SMX, 253 Da) and positively charged trimethoprim (TMP, 290 Da) is much lower than the MWCO of JM200, their rejection still reaches 80.6% and 85.5%, respectively, underscoring the significance of electrostatic exclusion (the Donnan effect) in enhanced rejection of charged EOCs. The decrease in MWCO of the JM slightly reduced antibiotic rejection due to size exclusion. For JM160 (MWCO = 726.4 Da), the rejection of TC and TOB was 93.8% and 98.1% (Fig. S11a), respectively, while it was still 90.7% and 92.1% for JM120 (MWCO = 880.3 Da) (Fig. S11b). Interestingly, JM160 and JM120 removed 79.5% and 73.9% of SMX, and 72.3% and 74.3% of TMP, respectively. Consequently, the JMs efficiently reject antibiotics possessing much lower MWs than their MWCO, demonstrating the robust rejection of antibiotics with different charge properties. Compared with JM200, JM160 and JM120 with higher permeability are feasible to retain larger MW pollutants. Consequently, the precise modulation of the membrane properties by controlling the 2D-MOF structures enables the efficient rejection of positively and negatively charged antibiotics.

For comparison, we determined the separation performance of single-sided membranes with the same thickness as the

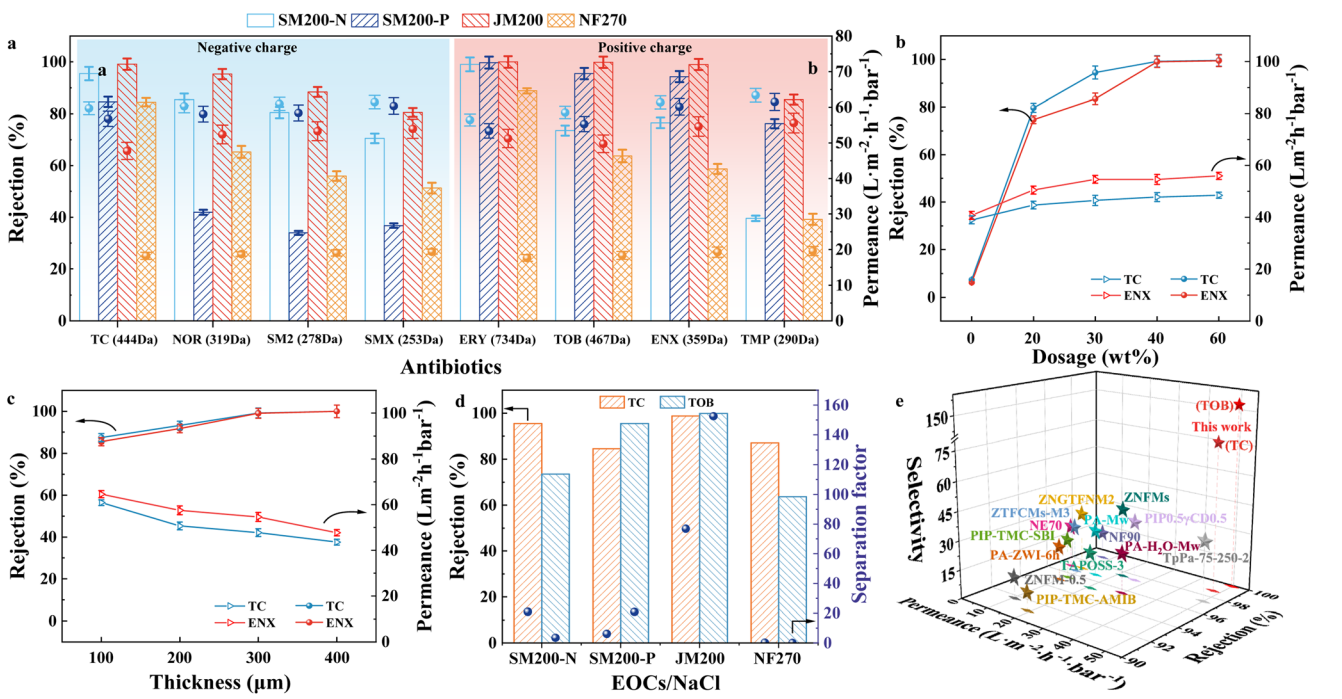

Fig. 2 Separation performance of JM. Rejection of typical antibiotics (a), the effect of 2D-MOF loading (b) and active layer thickness (c) on antibiotics removal by JM200 and the selective separation of antibiotics from inorganic salts (d), and comparison of JM200 with the commercial and state-of-the-art NF membranes (permeability, antibiotics rejection and antibiotics/NaCl selectivity) (e).

commercial NF membrane. Negatively charged SM200-N (MWCO = 605.3 Da) and positively charged SM200-P (MWCO = 572.5 Da) presented lower antibiotic removal than JM200 owing to their higher MWCO; moreover, they selectively reject antibiotics with the same charge property, while allowing the permeation of antibiotics with the opposite charge. For example, norfloxacin (NOR, MW = 319 Da) rejection still remained 85.4% by SM200-N, but markedly reduced to 41.9% by SM200-P. Similarly, TMP (MW = 290 Da) rejection reached 39.6% and 76.2% by SM200-N and SM200-P, respectively. Similar results were also observed for the SM160 (Fig. S11a) and SM120 membranes (Fig. S11b). Interestingly, commercial NF270 membrane with a low MWCO (223 Da) and negative charge (zeta potential = −58.3 mV at pH = 7 (ref. 26)) also exhibited poor rejection toward positively charged TMP (R = 39.2%) and enrofloxacin (ENX, MW = 359 Da, R = 58.7%), suggesting that size exclusion was insufficient for negatively charged NF270 to reject positively charged antibiotics owing to the electrostatic attraction. Nevertheless, the removal of negatively charged SMX (R = 51.3%) and sulfamethazine (SM2, MW = 278 Da, R = 55.9%) was also unsatisfactory by NF270, likely because the hydrophobic EOCs penetrated the PA membrane *via* a solution-diffusion mechanism.[27] Obviously, the inherent drawbacks of single charge membranes in terms of low removal of the opposite charged pollutants were overcome by the facile and precise design of an electrostatic Janus membrane without sacrificing permeability. Excitingly, JM200 displayed much superior permeability and antibiotic rejection than the single-sided membranes and commercial NF270 membranes, which further confirmed the superiority of the Janus structure. Besides, the single-sided SM200 also presented much higher water permeance and antibiotic rejection than NF270, underscoring the advantages of 2D-MOF membranes.

To better understand the role of the 2D-MOFs in membrane separation, we explored the effect of 2D-MOF loading amount in JM200 on antibiotic removal. The PVDF control membrane failed to repel TC and ENX with only 7.4% and 6.2% rejection, respectively (Fig. 2b), because the stochastic nature of the NIPS process caused a broader pore size distribution and formed defects within the PVDF matrix.[28] Excitingly, increasing the loading amount of 2D-MOFs (0–40 wt%) synchronously improved the permeability and antibiotic rejection (Fig. 2b). When the loading amount of the 2D-MOFs was up to 20 wt%, the TC and ENX rejection significantly enhanced to 79.7% and 74.7%, respectively; meanwhile, their water permeability increased from approximately 39 L per m^2 per h per bar (0 wt%) to 44.7 and 50.5 L per m^2 per h per bar. This phenomenon was because the 2D-MOFs narrowed the pore size of the JM (Fig. 1i), filled the defects within the membrane matrix, facilitated water transport and imparted the membrane with dually-charged properties, cooperatively causing superior permeability and rejection toward charged antibiotics.[12] Nevertheless, the antibiotic separation performance negligibly improved when the loading amount of 2D-MOFs was higher than 40 wt% due to the agglomeration of the 2D-MOFs.[29] Besides, the influence of functional layer thickness on membrane separation was also unveiled. Nowadays, designing ultrathin membranes (even 10 nm) is the mainstream method to break the permeability-selectivity trade-off.[30] However, scalable fabrication and avoiding defect formation are challenging in practical applications.[31] Intriguingly, increasing the functional layer thickness from 200 to 800 μm only decreased the permeability by approximately 17%, while TC and ENX rejection significantly increased to over 99.9% (Fig. 2c). This further verifies the low filtration resistance of JM200, attributed to the alveolar PVDF matrix, and the water pumping effect of the 2D-MOFs. Therefore, this study provides an alternative strategy to design high-performance NF membranes with micron thickness and a highly porous active layer in addition to the ultrathin and compact film.

Considering the coexistence of antibiotics and salt in many scenarios (*e.g.*, pharmaceutical wastewater), antibiotic selectivity is important for wastewater treatment and resource recovery. The separation factor of TOB/NaCl and TC/NaCl was up to 152 and 77 for JM200 (Fig. 2d), respectively, which was 55.9–148.9 times higher than that of the single-sided membranes (SM200-N and SM200-P). Moreover, the above separation factors were all below 0.3 for NF270 (Fig. 2d), attributed to its inadequate antibiotic rejection and superior salt rejection. Consequently, compared with NF270, which is designed for desalination, the fabricated JM was more feasible for the selective separation of antibiotics from salt or other pollutants (*e.g.*, heavy metals in aquaculture wastewater). Moreover, we compared the separation performance of JM200 with the previously reported NF membranes, such as commercial membranes (*e.g.*, NF270 and NF90), and state-of-the-art membranes (*e.g.*, PA, MOFs and covalent organic frameworks) (Fig. 2e). The detailed data are provided in Table S6. The JM200 membrane exhibits much higher permeability and selectivity toward both positively and negatively charged antibiotics, which further demonstrates the superiority of the 2D-MOF JM membrane for ultrafast and selective removal of EOCs owing to the porous matrix and designable 2D-MOFs.

The separation performance of JM200 was further explored for removing other types of EOCs. For EDCs (Fig. 3a), JM200 (MWCO = 442.7 Da) exceptionally rejected negatively charged 3,3,5,5-tetrabromobisphenol A (TBBPA, MW = 544 Da, R = 100%) and bisphenol AF (BPAF, MW = 336 Da, R = 96.4%), and neutrally charged bis(2-ethylhexyl)phthalate (DEHP, MW = 390 Da, R = 97.3%). Interestingly, although the MW of negatively charged bisphenol A (BPA, MW = 228 Da) and neutrally charged dibutyl phthalate (DBP, MW = 278 Da) was much lower than the MWCO of JM200, the rejection still remained at 73.5% and 92.0%, respectively. These phenomena suggested that, except for size exclusion, other interactions are also involved in the EOC separation mechanism, such as the Donnan effect and hydrophobic interactions. Similarly, JM200 realized complete rejection of long-chain PFAS heptadecafluorononanoic acid (PFNA, MW = 464 Da) and perfluorooctanoic acid (PFOA, MW = 414 Da) (Fig. 3a). Rejection of short-chain PFAS nonafluorobutane-1-sulfonic acid (PFBS, MW = 300 Da) and perfluorobutanoate (PFBA, MW = 214 Da) also remained at 94.0% and 70.4%, respectively. Also, for neutrally charged OPEs (Fig. 3a), tris(2-phenylphenyl)phosphate (TBPHP, MW = 555 Da) and tris(2-ethylhexyl)phosphate (TEHP, MW = 435 Da) with

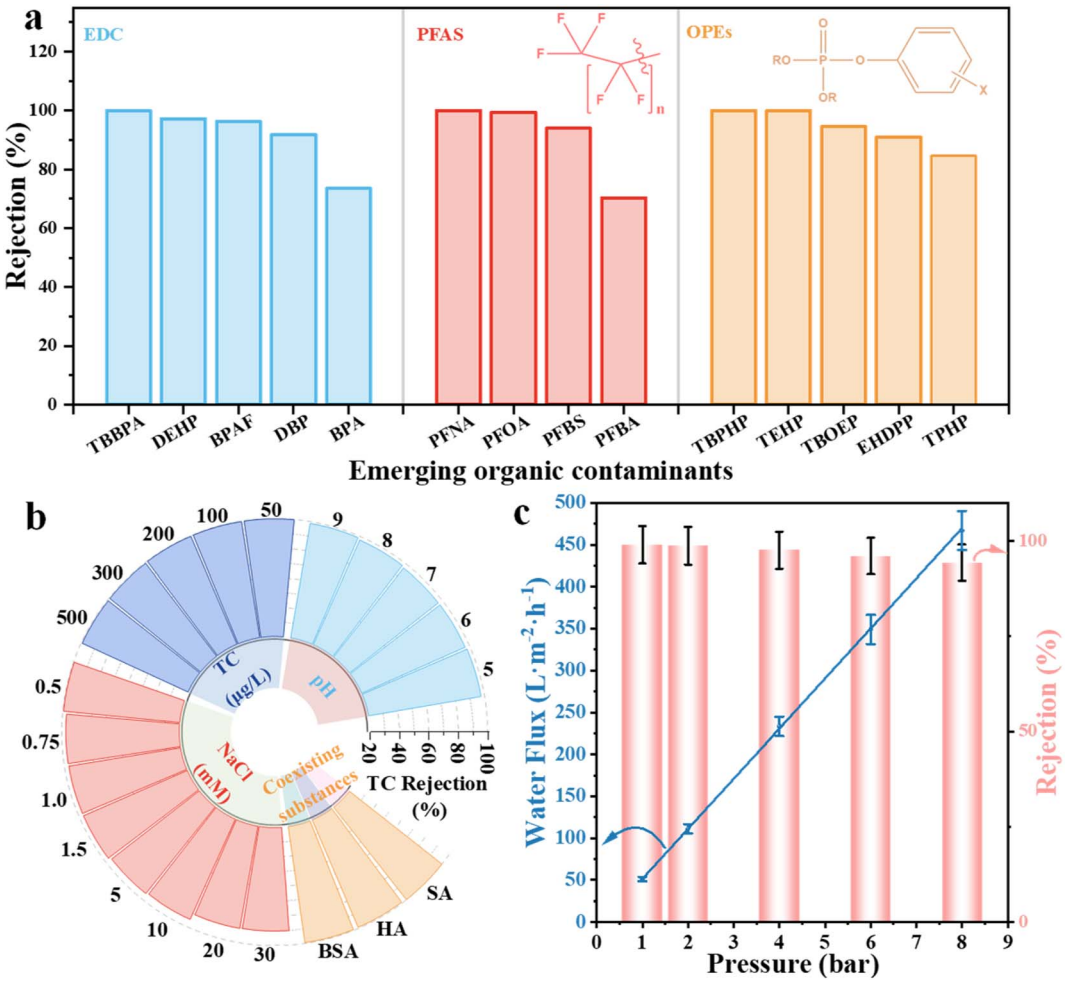

Fig. 3 Rejection of typical EDCs, PFAS, and OPEs by JM200 (a). Effect of water matrices (b) and operating pressure (c) on TC rejection by JM200.

a similar or higher MW than the MWCO of the membrane can be rejected completely. Moreover, rejection was also efficient for tris(2-butoxyethyl)phosphate (TBOEP, MW = 398 Da, R = 94.5%), 2-ethylhexyl diphenyl phosphate (EHDPP, MW = 362 Da, R = 91.1%) and triphenyl phosphate (TPHP, MW = 326 Da, R = 84.7%), although their MWs were lower than the MWCO of the membrane. Excitingly, JM200 enabled broad-spectrum rejection of various EOCs with different sizes, charges and hydrophobicities, even for small EOCs with a much lower MW than the membrane MWCO due to the multiple rejection mechanisms as unveiled hereinafter.

The influence of water matrices and operating pressure on separation performance was further explored to evaluate the practical applicability. JM200 exhibits robust anti-interference performance without compromising TC rejection over wide ranges of pH (5–9), initial antibiotic concentrations (50–500 μg L^{-1}), salt concentrations (<10 mM) and coexisting organic macromolecules (BSA, HA and SA) (Fig. 3b), which further demonstrated its great potential in EOC removal from complex water matrices. When the salt concentration was higher than 10 mM, the TC rejection slightly reduced owing to the charge shielding effect.[32] However, the TC rejection was only sacrificed by approximately 9% even at 30 mM NaCl, suggesting that the separation performance was maintained in moderate salinity water matrices (*e.g.*, surface water and municipal wastewater). Besides, water flux almost linearly enhanced with increasing operating pressure, while TC rejection negligibly attenuated (Fig. 3c), suggesting that JM200 was tolerant to a wide pressure range.[12] Moreover, the water flux still remained at 51.2 L m^{-2} h^{-1} at 1 bar, which confirmed that JM200 was feasible for operating under low applied pressure, thereby reducing energy consumption, membrane fouling and concentration polarization.

Separation mechanism exploration

To understand the separation mechanism, we conducted correlation analysis between the physicochemical properties of the EOCs (MW, pK_a and hydrophobicity) and the separation performance of JM200. The correlation coefficients (r) for different kinds of EOC are illustrated in Fig. 4. The MW (r = 0.79) and Stokes' radius (R_s, r = 0.75) of the antibiotics presented a positive and high correlation with the rejection rate, while it was low for pK_a (r = 0.32) and log K_{ow} (r = −0.31). Consequently, size exclusion played an important role in antibiotic rejection. The weak correlation with pK_a likely originated from the unique charge-asymmetric bilayer structure of the

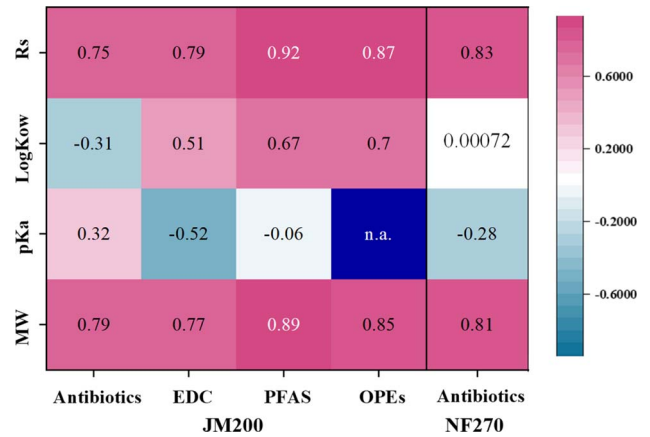

Fig. 4 Correlation between EOC properties (MW, pK_a, log K_{ow} and R_s) and rejection performance by the JM200 and NF270 membranes.

electrostatic Janus membrane. While electrostatic interactions played a secondary role, the electrostatic Janus structure enabled the effective rejection of positively and negatively charged antibiotics through the Donnan effect. Comparatively, antibiotics rejection by NF270 also presented high correlation with MW ($r = 0.81$) and R_s ($r = 0.83$), followed by low correlation with pK_a ($r = -0.28$) and no correlation with log K_{ow} ($r = 0.00071$). Similar to JM200, NF270 mainly rejected antibiotics by size exclusion. However, NF270 poorly removed positively charged antibiotics owing to electrostatic attraction. Notably, hydrophobic interaction fails to work for NF270, responsible for its inferior EOC rejection performance than JM200. Interestingly, the water contact angle of NF270 (40°)[33] was lower than that of JM200 (53.2°), which cannot explain the above results. Notably, the water contact angles of MgAl–BDC–NH_2-200 and MgAl–BDC-200 were only 15.5° and 23.6°, respectively (Fig. S12). Thus, we proposed that the hydrophilic 2D-MOFs that were incorporated into the hydrophobic PVDF matrix provided the main separation channels for antibiotics rejection, which was consistent with the impact of 2D-MOF loading amount on separation performance (Fig. 2b).

Similar to antibiotics, the MW ($r = 0.76$) and R_s ($r = 0.79$) of EDCs exhibited high correlation with rejection rate, followed by log K_{ow} ($r = 0.51$) and pK_a ($r = -0.52$) (Fig. 4). Compared with antibiotics, the higher correlation of log K_{ow} and pK_a with EDC rejection indicated that electrostatic and hydrophobic interactions were also involved in EDC rejection, in addition to size exclusion. Moreover, JM200 favored the rejection of EDCs with more acidity and hydrophobicity owing to the stronger electrostatic repulsion and weaker hydrophobic attraction.[16] Additionally, PFAS rejection has a high and positive correlation with their MW ($r = 0.89$) and log K_{ow} ($r = 0.67$), but poor correlation with pK_a ($r = -0.059$) (Fig. 4), suggesting that the PFAS rejection mechanism was mainly governed by size exclusion and hydrophobic interactions. The hydrophobic PFAS presented weak hydrophobic attraction with hydrophilic JM200, making them easier for the membrane to retain.[34] Similar to PFAS, OPE rejection exhibited high and positive correlation with MW ($r = 0.85$) and log K_{ow} ($r = 0.70$), suggesting that the OPE rejection mechanism was due to the synergy of size exclusion and hydrophobic interaction. Notably, OPEs were not ionized or hydrolyzed at neutral pH,[35] and thus their uncharged property caused the lack of the Donnan effect.

In summary, the rejection of EOCs by JM200 was governed by their structural features and properties, causing different rejection mechanisms for the different types of EOC. Therefore, the matching relation between the EOCs and 2D-MOF JM was unveiled to guide the broad-spectrum rejection of EOCs.

In addition, membrane transport principles were employed to understand the rejection mechanism of the EOCs. Taking negatively charged TC as an example, the fitting results of the experimental data with Ferry's model, the Donnan model, and the Donnan-Steric pore model are illustrated in Fig. 5a–c. Among them, Ferry's model and the Donnan model reflected the size exclusion and Donnan exclusion mechanism, respectively,[36,37] while the Donnan-Steric pore model combined size exclusion and Donnan exclusion.[38] Obviously, TC rejection presented poor relevance with Ferry's model (Fig. 5a) and the Donnan model (Fig. 5b), suggesting that the TC rejection mechanism was not governed by single size exclusion or Donnan exclusion. Instead, TC rejection was well fitted with the Donnan-Steric pore model (Fig. 5c), which confirmed the synergistic rejection mechanism of size exclusion and Donnan exclusion. Then, three EOCs with a lower MW than the MWCO of JM200 were selected to unlock the separation mechanism, including positively charged and hydrophilic TMP (MW = 290 Da, log $K_{ow} = 0.73$) and ENX (MW = 359 Da, log $K_{ow} = 0.70$), and positively charged and hydrophobic bezafibrate (BEZ, MW = 362 Da, log $K_{ow} = 4.25$). Firstly, the Donnan effect was excluded by separation at high salinity (10 g per L NaCl), and the rejection of TMP, ENX and BEZ was reduced by 17.0%, 21.7% and 11.8%, respectively (Fig. 5d), revealing the important role of the Donnan effect. Furthermore, although ENX and BEZ possessed similar MWs, BEZ rejection increased slightly by 8.4% compared to ENX at high salinity, confirming the notable role of hydrophobic interactions. Additionally, the rejection of TMP and ENX with similar log K_{ow} values still remained at 68.4% and 77.3% at high salinity, further emphasizing the dominant effect of size exclusion.

Overall, we unveiled the separation mechanism from the aspects of membrane and EOC structure (Fig. 6). Benefiting from the Janus structure and 2D-MOF feature, JM200 achieves high permeability and broad-spectrum rejection of EOCs. The electrostatic Janus structure realized the efficient rejection of positively and negatively charged EOCs *via* electrostatic exclusion, which solved the low permeability and rejection of positively charged EOCs of conventional PA TFC membranes with a compact and negatively charged active layer; meanwhile, the porosity and hydrophilic nature of the 2D-MOFs allowed for rejection of neutrally charged and hydrophobic EOCs by the Janus membrane. Furthermore, EOCs with different structures and properties contained varied rejection sites and domains (Fig. 6), causing different interactions with the membrane and separation mechanisms.

Membrane anti-fouling performance

The anti-fouling performance of the JM membranes was assessed using BSA, SA and HA as model foulants. To

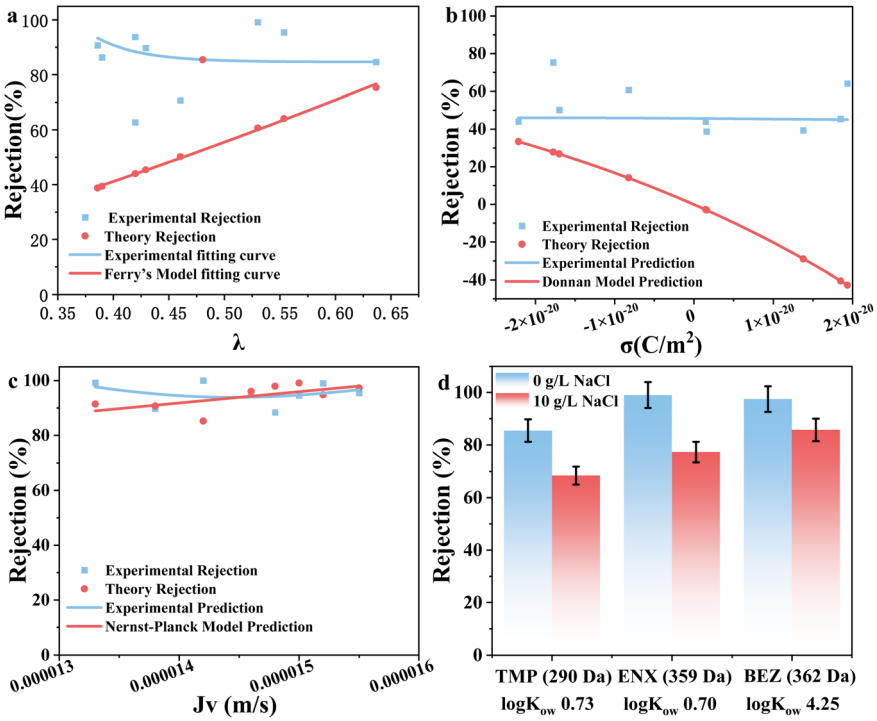

Fig. 5 Experimental and theoretical data for TC rejection by membrane fitting with Ferry's model (a), the Donnan model (b) and the Donnan-Steric pore model (c). λ is the relative size parameter defined as the ratio of the solute size to the membrane pore size, σ is the charge density (C m^{-2}), and J_v is the volumetric flux (m s^{-1}). Rejection of typical EOCs by JM200 at high salinity (10 g per L NaCl) (d).

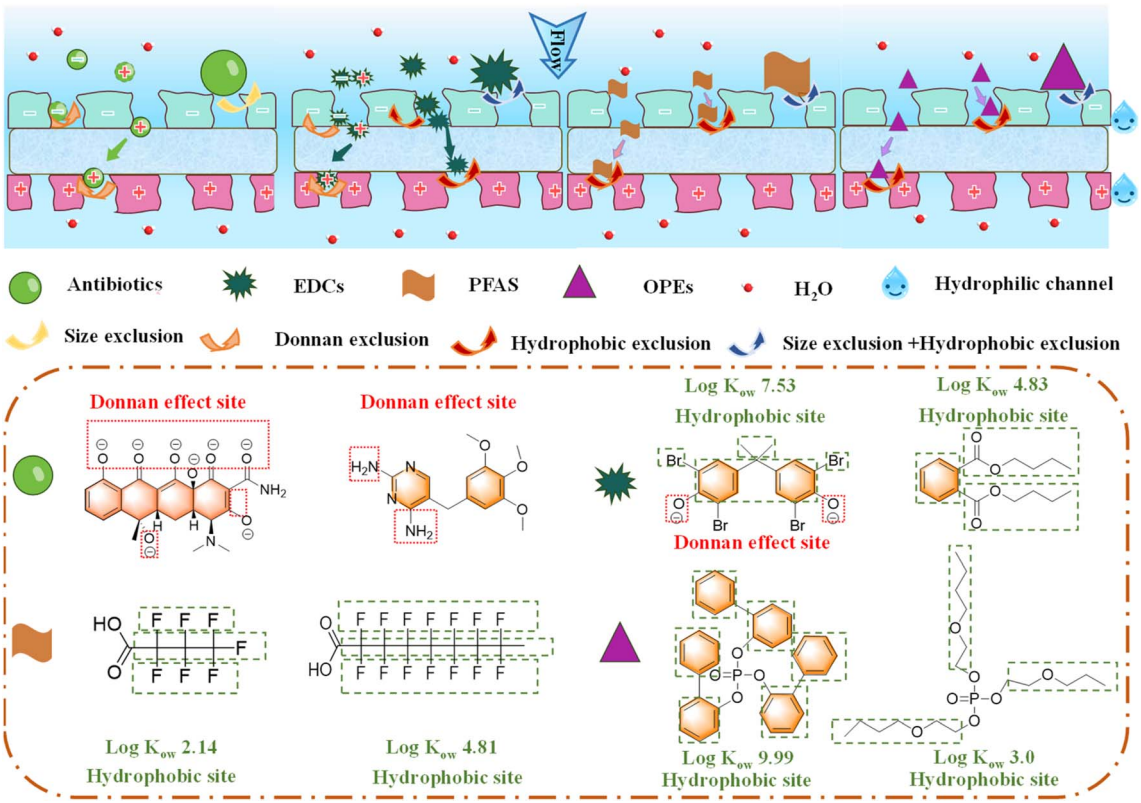

Fig. 6 Separation mechanism toward different kinds of EOCs by JM200.

investigate the anisotropic anti-fouling properties of JM200, filtration experiments were conducted with the opposite feed orientations. Significantly, the normalized flux (J_N) loss was 42.5% after 90 min of filtration of BSA through the JM200-N feed orientation, while it increased to 49.8% for JM200-P (Fig. 7a), originating from the different electrostatic interactions between the membranes and negatively charged BSA. In comparison, J_N reduced by 49.5% and 67.4%, respectively, for single-sided SM200-N and SM200-P. Obviously, JM200 exhibited less flux loss than SM200 and other JMs (JM120 and JM160, Fig. S11), attributed to their smaller pore sizes (Fig. 1i) and more negative charge (Fig. 1g).[39] Furthermore, after hydraulic washing, the feed directions toward JM200-N achieved the highest flux recovery rate (FRR, 90.7%) and lowest irreversible fouling ratio (R_{ir}, 9.28%) (Fig. 7b), implying outstanding anti-fouling ability. However, FRR and R_{ir} increased to 76.6% and 23.4%, respectively, for the JM200-P feed direction. The superior anti-fouling mechanism (Fig. 7c) for the feed direction toward JM200-N was due to the stronger electrostatic repulsion and weaker hydrophobic attraction between the membrane and foulants.[14] In addition, this phenomenon was also observed for fouling by SA (Fig. S13) and HA (Fig. S14). Notably, SA fouling was more severe than BSA and HA fouling with more flux decline likely due to the stronger interaction of SA with the membrane, while JM200 still presented high flux recovery and fouling reversibility. The SEM images further revealed significantly less accumulation of foulants on the JM200-N surface compared with JM200-P before and after cleaning (Fig. S15). Moreover, this variation was more significant and fouling was more severe for SM200 than JM200. Specifically, FRR and R_{ir} reached 80.1% and 19.9% for SM200-N, and 74.7% and 25.3% for SM200-P, respectively. Similar results were observed for JM120, JM160 and the corresponding SM membranes (Fig. S16), suggesting that the 2D-MOF JM membranes exhibit good anti-fouling ability owing to their hydrophilic and negative properties. The feed direction largely influenced the fouling performance, which solved the severe fouling issues of positively charged NF membranes.

Chlorine resistance property

We further compared the chlorine resistance properties of the JM200 and NF270 membranes by determining their separation performance after exposure to NaClO. The NF270 permeability sharply increased with increasing chlorination treatment, accompanied by a decline in TC rejection (Fig. 8a). After exposure to a cumulative chlorine dose of 250 000 ppm min, the TC rejection decreased by 19.8%, indicating severe membrane degradation under oxidative conditions as the amide N–H groups on PA converted to N–Cl by reactive chlorine *via* amino chlorination reaction.[40] The SEM images also revealed the damage to the NF270 membrane after chlorine exposure (Fig. 8b and c). In contrast, JM200 exhibited excellent oxidation resistance as the separation performance remained constant (Fig. 8a), and the morphology negligibly changed (Fig. 8d and e) even under harsh chlorine treatment (400 000 ppm min). Besides, we also evaluated the dynamic cross-flow chlorine

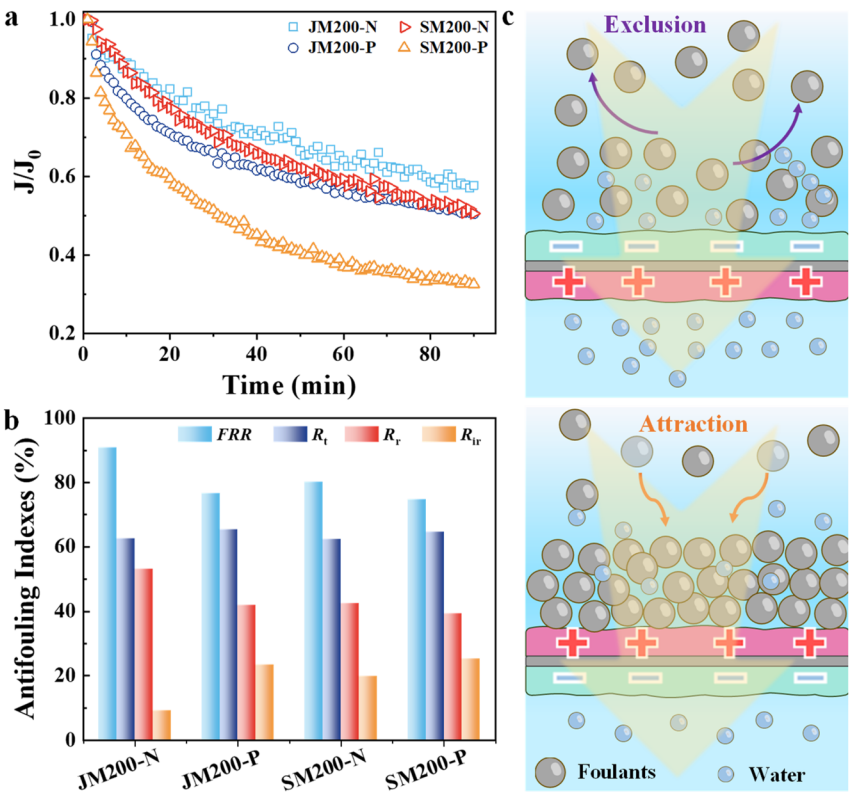

Fig. 7 Anti-fouling performance of the membranes. Normalized flux (a) and fouling resistance (b) of the Janus and single-sided membranes after fouling by BSA (100 mg L^{-1}). Anti-fouling mechanism of the Janus membrane from different feed directions (c).

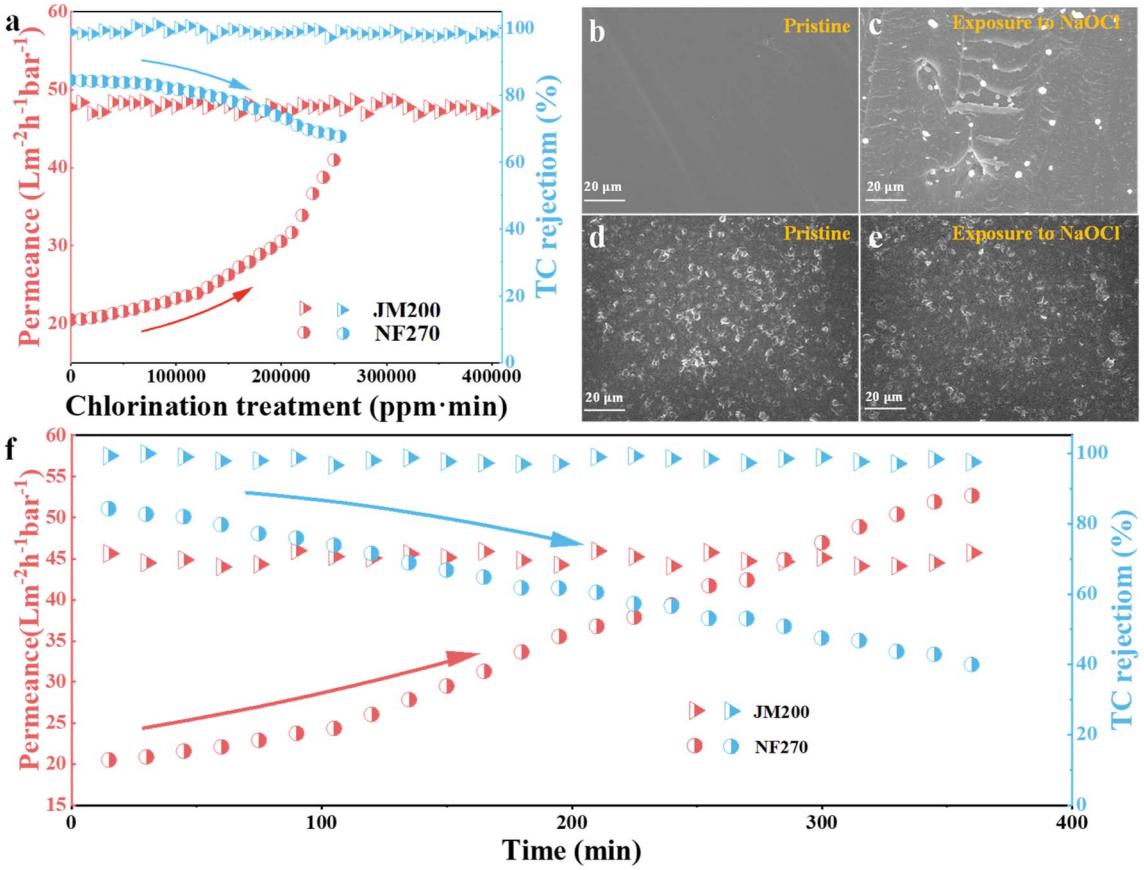

Fig. 8 Chlorine resistance of the membranes. Separation performance of JM200 and NF270 after exposure to NaOCl solution at neutral pH for filtration of TC (a), SEM images of the NF270 (b and c) and JM200 (d and e) surfaces before and after exposure to NaOCl, and dynamic cross-flow chlorine resistance tests of JM200 and NF270 for filtration of TC solution containing NaClO (50 mg L^{-1}) under a pressure of 0.2 MPa (f).

resistance of the membranes for 6 h. The TC rejection remained constant for JM200, while it significantly reduced to only 39.9% for NF270 (Fig. 8f). Consequently, similar to the chlorine resistance in the static immersion test, JM200 also presented superior chlorine resistance than NF270 during dynamic cross-flow chlorine resistance tests. The exceptional chlorine resistance of JM200 is attributed to the protection of the 2D-MOFs from oxidation damage by the PVDF matrix with strong covalent bonds and high hydrophobicity,[41] which resolved the poor chlorine resistance of the PA membrane and favored biofouling control.

Application in water remediation and reclamation

To evaluate the practical applicability of JM200 in water treatment, long-term filtration tests were performed by filtering two surface water samples and one municipal wastewater sample. JM200 demonstrated exceptional and stable separation performance for continuous filtration of these water matrices for 7 days (Fig. 9a). For Caiyue Lake water, the rejection of TBBPA and BEZ was as high as 100% and 97.6% (Fig. 9a), respectively, suggesting that EOC rejection was still outstanding in practical water treatment. Furthermore, the permeate met the Chinese surface water standard (GB3838-2002, Grade II) in terms of chemical oxygen demand (COD), biochemical oxygen demand (BOD) and ions (Table S7), suggesting that JM200 enabled the synergistic removal of EOCs and conventional pollutants due to its efficient separation ability. Additionally, excitation–emission matrix (EEM) analysis revealed that the fluorescence intensity of natural organic matter (NOM) in Caiyue Lake water markedly weakened after JM200 filtration (Fig. 9d–f). Furthermore, parallel factor analysis (PARAFAC) categorized the dissolved fluorescent organics into three fractions[42] (Fig. S17): C1 (humic-like substance), C2 (tryptophan protein-like substance), and C3 (tyrosine protein-like substance).[43] Remarkably, JM200 exhibited superior removal efficiencies of 89.7%, 100%, and 98.4% for components C1, C2, and C3 compared to the commercial NF270 membrane, respectively (Fig. 9g), demonstrating its outstanding capability for the rejection of fluorescent organic matter (FOM). Generally, FOM is considered as a precursor of carcinogenic disinfection by-products.[44] Consequently, JM200 filtration is beneficial for drinking water safety. Besides, the negligible leaching (<0.01 mg L^{-1}) of Al and Mg in the permeate after deducting the environmental background (Fig. S18) indicated the high stability of the membrane.

The FRR of JM200 was still maintained at 98.7% after seven consecutive filtration-hydraulic cleaning cycles without chemical cleaning (Fig. 10a); moreover, the ATR-FTIR spectra (Fig. S19a), photos (Fig. 10b and c) and SEM (Fig. 10d and e) analysis further revealed that JM200 after hydraulic cleaning

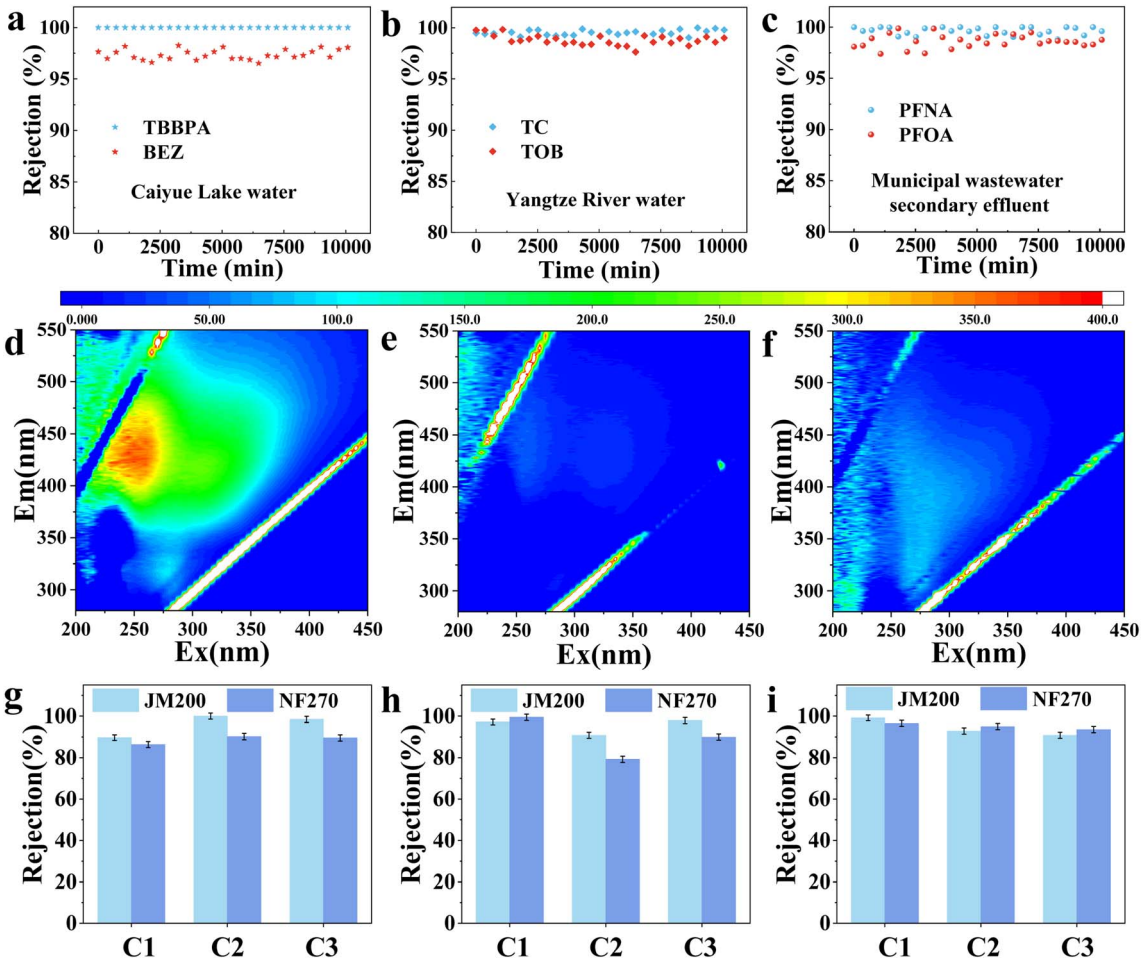

Fig. 9 Rejection of EOCs in Caiyue Lake water (a), Yangtze River water (b) and municipal wastewater secondary effluent (c) by JM200 for long-term filtration. EEM spectra of fluorescent organic matter in raw Caiyue Lake water (d), and permeates of JM200 (e) and NF270 (f). Rejection of three fluorescent components (C1, C2, and C3) extracted from the EEM spectra of Caiyue Lake water (g), Yangtze River water (h) and municipal wastewater secondary effluent (i) by PARAFAC analysis.

exhibited spectra and morphologies nearly identical to the pristine one, demonstrating its excellent anti-fouling and regeneration performance. Notably, peaks corresponding to –N–H and –C–O appeared on JM200 after fouling by Caiyue Lake water according to the ATR-FTIR spectra, likely indicating that protein-like and polysaccharide-like substances were the main foulants responsible for membrane fouling. Besides, JM200 achieved complete rejection of bacteria (Fig. S20a–c). Laser scanning confocal microscopy (LSCM) analysis also illustrated that live bacteria (Fig. 10f) on the membrane surface were all killed by chlorine pretreatment (Fig. 10g), indicating that chlorine-resistant JM200 favored biofouling control by impeding bacterial proliferation.

To verify general applicability, extended 7 day evaluations were also conducted using other water matrices. For the Yangtze River water, coagulation pretreatment using $AlCl_3$ coagulant was conducted to remove macromolecular organic matter for membrane fouling mitigation. Notably, coagulation failed to remove antibiotics (Table S8), while JM200 filtration enabled exceptional removal of TC (99.6%), TOB (99.1%) (Fig. 9b), and bacteria (100%) (Fig. S20d–f). Fluorescent organics removal was 90.8–97.9% (Fig. 9h) according to PARAFAC analysis (Fig. S21). Furthermore, the permeate water quality also met the Chinese surface water standard (GB3838-2002, Grade II) (Table S8), which also confirmed its great potential in surface water remediation. Similar to Caiyue Lake water, flux recovery was up to 99.3% by hydraulic cleaning after seven cycles (Fig. 10a). ATR-FTIR spectra (Fig. S19b) revealed the characteristic peaks of –COO^- and –C–O for JM200 after fouling by Yangtze River water, suggesting that humic acid-like and polysaccharide-like substances were the main foulants. Additionally, the functional groups (Fig. S19b) and surface morphologies (Fig. S22a and b) of JM200 were almost restored after hydraulic cleaning, further demonstrating its high anti-fouling and self-cleaning ability in the remediation of different surface water matrices. Besides, for municipal wastewater secondary effluent, JM200 effectively rejected PFNA (R = 99.6%), PFOA (R = 98.6%) (Fig. 9b) and bacteria (R = 100%) (Fig. S20d–f). The fluorescent organic component removal was >89.7% (Fig. 9i) based on PARAFAC analysis (Fig. S23). Moreover, it simultaneously removed conventional pollutants, and the permeate water met the Chinese municipal water reuse standard for urban

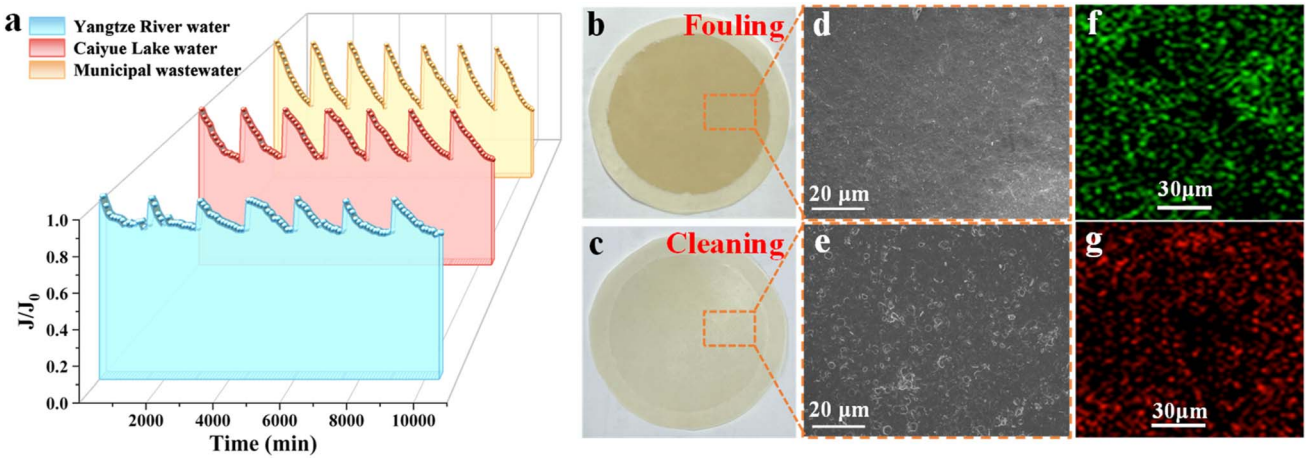

Fig. 10 Membrane performance in practical water treatment. JM200 flux curve during long-term filtration of complex water matrices (a), photos (b and c) and SEM images (d and e) of the JM200 surface after fouling and self-cleaning, and LSCM images of bacteria on the JM200 surface before (f) and after (g) chlorine treatment.

miscellaneous use (GB/T 18920-2020) (Table S9). The above phenomena demonstrated that JM200 enabled the broad-spectrum removal of EOCs from different water matrices. Notably, flux decline during municipal wastewater treatment was 14–29% greater than that during surface water treatment (Fig. 10a), attributed to the presence of more foulants (Tables S2–S4). Moreover, the ATR-FTIR spectra of JM200 after fouling by municipal wastewater secondary effluent in Fig. S19c illustrated the characteristic peaks of –N–H and $-COO^-$, revealing that protein-like foulants tended to accumulate on the membrane surface. However, after hydraulic cleaning, the flux recovery rates remained above 94.7%. The ATR-FTIR spectra (Fig. S19c) and SEM images (Fig. S22c and d) also confirmed the recovery of the membrane functional groups and morphologies, revealing the robust anti-fouling capability of JM200. These findings present a feasible strategy for EOC removal and safeguarding water quality safety.

Conclusion

This study customizes 2D-MOF chlorine-resistant Janus NF membranes for ultrafast and broad-spectrum removal of antibiotics, EDCs, PFAS and OPEs with different structures, charges and hydrophobic properties, thereby addressing the inherent drawbacks of conventional membranes. Incorporating designable 2D-MOFs within an alveolar PVDF matrix imparted Janus membranes with exceptional water permeability and EOC rejection under low operating pressures. The correlation between EOC properties and the separation performance of the JM200 membrane, membrane transport principles and electrostatic shielding tests confirmed the important role and multiple mechanisms of electrostatic Janus structures, and the porosity and hydrophilic nature of the 2D-MOFs in EOC rejection. Furthermore, the 2D-MOF Janus membrane exhibited efficient anti-fouling, chlorine resistance, stability and economic feasibility in the long-term treatment of complex water matrices, making it an ideal candidate for sustainable water treatment. The preparation process of 2D-MOF Janus membranes can be further simplified by coating both sides of the active layer simultaneously using double-sided coating equipment.

Author contributions

Z. Hu; data curation, formal analysis, writing-original draft. K. Tian; data curation, formal analysis, writing-original draft. L. Li; formal analysis. H. Dai; formal analysis. Z. Peng; formal analysis. Z. Yin; conceptualization, funding acquisition, resources, supervision, writing-review & editing. W. Yang; writing-review & editing.

Conflicts of interest

There are no conflicts to declare.

Data availability

The data supporting this article have been included as part of the supplementary information (SI). Supplementary information: experimental details, characterization data, membrane performance, additional figures and tables. See DOI: **https://doi.org/10.1039/d5sc05978j**.

Acknowledgements

This research was financially funded by the National Natural Science Foundation of China (No. 52200058), and Natural Science Foundation of Jiangsu Province (No. BK20220380).

References

1 J. Cai, B. Niu, Q. Xie, N. Lu, S. Huang, G. Zhao and J. Zhao, *Environ. Sci. Technol.*, 2022, **56**, 2917–2935.

2 J. Garcia-Ivars, L. Martella, M. Massella, C. Carbonell-Alcaina, M. I. Alcaina-Miranda and M. I. Iborra-Clar, *Water Res.*, 2017, **125**, 360–373.
3 D. Li, W. Liu, X. Wang, W. Lin, J. Zhai, H. Fan, K. Xiao, K. Wang, Y. Li, Y. Jin, J. Fang, Y. Shen, M. Elimelech and X. Huang, *Sci. Adv.*, 2025, **11**, eadt3324.
4 R. Dai, X. Wang, C. Y. Tang and Z. Wang, *Environ. Sci. Technol.*, 2020, **54**, 7619–7628.
5 A. R. D. Varied, E. R. Cornelissen, S. G. J. Heijman, J. Q. J. C. Verberk, G. L. Amy, B. Van der Bruggen and J. C. van Dijk, *J. Membr. Sci.*, 2008, **322**, 52–66.
6 Y. Yao, P. Zhang, F. Sun, W. Zhang, M. Li, G. Sha, L. Teng, X. Wang, M. Huo, R. M. DuChanois, T. Cao, C. Boo, X. Zhang and E. Menachem, *Science*, 2024, **384**, 333–338.
7 S. Zhao, C. Ba, Y. Yao, W. Zheng, J. Economy and P. Wang, *Chem. Eng. J.*, 2018, **335**, 101–109.
8 X. Bao, Q. She, W. Long and Q. Wu, *Water Res.*, 2021, **190**, 116678.
9 Z. Liu, H. Wen, S. Jiang, J. Xu and J. P. Chen, *Desalination*, 2025, **597**, 118316.
10 X.-Y. Guo, L. Zhao, H.-N. Li, H.-C. Yang, J. Wu, H.-Q. Liang, C. Zhang and Z.-K. Xu, *Science*, 2024, **386**, 654–659.
11 K. Zhang, P. Cheng, Y. Liu and S. Xia, *Water Res.*, 2024, **265**, 122276.
12 H. Yu, Y. Liu, Z. Yin and W. Yang, *J. Membr. Sci.*, 2025, **733**, 124289.
13 Z. Hu, Z. Yin, F. Guo and W. Yang, *J. Membr. Sci.*, 2023, **686**, 122026.
14 Z. Hu, Z. Yin, Y. Chen, T. Wen, F. Li and W. Yang, *J. Membr. Sci.*, 2024, **709**, 123108.
15 H. G. Alemayehu, C. Liu, J. Hou, J. Yang, M. Fang, Z. Tang and L. Li, *J. Membr. Sci.*, 2022, **652**, 120479.
16 Z. Yin, Y. Liu, Z. Hu, J. Wang, F. Li and W. Yang, *J. Hazard. Mater.*, 2024, **475**, 134944.
17 Y. Ren, P. Qi, Y. Wan, C. Chen, X. Chen, S. Feng and J. Luo, *Environ. Sci. Technol.*, 2022, **56**, 18018–18029.
18 X. Xu, J. Wang, A. Zhou, S. Dong, K. Shi, B. Li, J. Han and D. O'Hare, *Nat. Commun.*, 2021, **12**, 3069.
19 M. Han, X. Zhang, H. Gao, S. Chen, P. Cheng, P. Wang, Z. Zhao, R. Dang and G. Wang, *Chem. Eng. J.*, 2021, **426**, 131348.
20 B. P. Carpenter, A. R. Talosig, B. Rose, G. Di Palma and J. P. Patterson, *Chem. Soc. Rev.*, 2023, **52**, 6918–6937.
21 A. Miao, M. Wei, F. Xu and Y. Wang, *J. Membr. Sci.*, 2020, **604**, 118087.
22 Y. Zhao, F. Kong, Z. Wang, H. Yang, X. Wang, Y. F. Xie and T. D. Waite, *Front. Environ. Sci. Eng.*, 2017, **11**, 20.
23 M. Jian, R. Qiu, Y. Xia, J. Lu, Y. Chen, Q. Gu, R. Liu, C. Hu, J. Qu, H. Wang and X. Zhang, *Sci. Adv.*, 2020, **6**, 3998.
24 W. Guo, H.-H. Ngo and J. Li, *Bioresour. Technol.*, 2012, **122**, 27–3.
25 C. R. Marshall, S. A. Staudhammer and C. K. Brozek, *Chem. Sci.*, 2019, **10**, 9396–9408.
26 J. Guo, M. U. Farid, E.-J. Lee, D. Y.-S. Yan, S. Jeong and A. K. An, *J. Membr. Sci.*, 2018, **551**, 12–19.
27 X. Chen, J. Ren, Z. Wang and X. Tong, *Desalination*, 2025, **611**, 118938.
28 J. R. Werber, C. O. Osuji and M. Elimelech, *Nat. Rev. Mater.*, 2016, **1**, 1–15.
29 L. Shu, L.-H. Xie, Y. Meng, T. Liu, C. Zhao and J.-R. Li, *J. Membr. Sci.*, 2020, **603**, 118049.
30 T. Huang, B. A. Moosa, P. Hoang, J. Liu, S. Chisca, G. Zhang, M. AlYami, N. M. Khashab and S. P. Nunes, *Nat. Commun.*, 2020, **11**, 5882.
31 J. R. McCutcheon and M. S. Mauter, *Science*, 2023, **380**, 242–244.
32 J. Lin, W. Ye, S. Xie, J. Du, R. Liu, D. Zou, X. Chen, Z. Yu, S. Fang, E. Y. M. Ang, W. Toh, D. D. Han, T. Y. Ng, D. H. Seo, S. Zhao, B. Van der Bruggen, M. Xie and Y. M. Lee, *Nat. Water*, 2023, **1**, 725–735.
33 C. Bellona, M. Marts and J. E. Drewes, *Sep. Purif. Technol.*, 2010, **74**, 44–54.
34 F. Fang, S. Chen, K. Shi, S. Xu, Z. Yi, L. Lei, L. Zhuang, H. Wan and Z. Xu, *Sep. Purif. Technol.*, 2024, **348**, 127379.
35 P. Bhatt, X. Zhou, Y. Huang, W. Zhang and S. Chen, *J. Hazard. Mater.*, 2021, **411**, 125026.
36 R. Xu, Z. Zhang, C. Deng, C. Nie, L. Wang, W. Shi, T. Lyu and Q. Yang, *Environ. Res.*, 2024, **244**, 117935.
37 J. Waniewski, M. Pietribiasi and L. Pstras, *Sci. Rep.*, 2021, **11**, 22150.
38 R. Wang and S. Lin, *J. Membr. Sci.*, 2021, **620**, 118809.
39 Z. Dai, P. Jin, S. Yuan, J. Yang, K. V. Agrawal and H. Wang, *Nat. Commun.*, 2025, **16**, 4626.
40 X. Geng, J. Wang, Y. Ding, W. Zhang, Y. Wang and F. Liu, *J. Membr. Sci.*, 2021, **632**, 119385.
41 P. Huang, C. Chen, M. Gu, G. Yang, Y. Gao, H. Ding, S. Liang and X. Huang, *J. Membr. Sci.*, 2025, **719**, 123749.
42 T. Maqbool, J. Zhang, Y. Qin, Q. V. Ly, M. B. Asif, X. Zhang and Z. Zhang, *Water Res.*, 2020, **183**, 116096.
43 H. Lin and L. Guo, *Environ. Sci. Technol.*, 2020, **54**, 1657–1667.
44 Y. Xia, Y.-L. Lin, B. Xu, C.-Y. Hu, Z.-C. Gao, Y.-L. Tang, W.-H. Chu, T.-C. Cao and N.-Y. Gao, *Water Res.*, 2018, **147**, 101–111.